RESEARCH ARTICLE
SOLID EARTH: GEOELECTROMAGNETICS

Earth and Planetary Physics
9: 622–634, 2025
doi: 10.26464/epp2025064

A cubed-sphere based method for global and regional modeling of the lithospheric magnetic field

Liang Yin[1*], JiaXuan Zhang[1,3], PengFei Liu[1*], HongBo Yao[1], Pan Zhang[2], and JinSong Du[2]

[1]Macau Institute of Space Technology and Application, Macau University of Science and Technology, Macao 999078, China;

[2]Hubei Subsurface Multi-scale Imaging Key Laboratory, School of Geophysics and Geomatics, China University of Geosciences, Wuhan 430074, China;

[3]Institute of Space Weather, School of Atmospheric Physics, Nanjing University of Information Science & Technology, Nanjing 210044, China.

Key Points:

- A new equivalent dipole method based on cubed-sphere grid is proposed for lithospheric field modeling.
- The modeling methods including forward approaches and inversion procedure are adequately validated by several synthetic cases.
- The proposed method is successfully applied to build global and regional models from *Swarm Alpha* and MSS-1 satellite magnetic data.

Citation: Yin, L., Zhang, J. X., Liu, P. F., Yao, H. B., Zhang, P., and Du, J. S. (2025). A cubed-sphere based method for global and regional modeling of the lithospheric magnetic field. *Earth Planet. Phys.*, *9*(3), 622–634. http://doi.org/10.26464/epp2025064

Abstract: The Earth's magnetic field, which has been extensively observed from ground to satellite altitudes over several decades, originates from multiple sources, such as the core dynamo, the conductive mantle, the magnetized lithosphere, and the space current systems. Modeling of the lithospheric contribution plays an important role in the geophysical studies and industrial applications. In this paper, we propose a new method for global and regional modeling of the lithospheric magnetic field based on the cubed-sphere. An equivalent dipole source method on a quasi-uniform cubed-sphere grid is employed in the forward modeling. The dipole directions are fixed according to a priori magnetization and the relative intensities are estimated by an inversion procedure of least-squares fitting with minimum model regularization. Several numerical tests are performed to validate the accuracy and efficiency of both forward modeling and inversion procedure. The proposed method is applied to the global and regional modeling based on the latest magnetic data from *Swarm Alpha* satellite and MSS-1 mission. The model results indicate that the proposed method works quite well for realistic satellite data and MSS-1 data is consistent with the *Swarm* data in terms of lithospheric field modeling.

Keywords: geomagnetic satellite; lithospheric magnetic field; cubed-sphere grid; forward modeling; inversion

1. Introduction

The Earth's magnetic field has been extensively observed from ground to satellite altitudes over several decades. The geomagnetic measurement data above the surface originates from multiple sources, such as the core dynamo, the electrically conductive mantle, the magnetized lithosphere and the space current systems (Zhang K, 2023; Ren ZY et al., 2025). According to the observation data, a number of geomagnetic field models have been constructed (Olsen et al., 2017; Finlay et al., 2020; Sabaka et al., 2020) and significantly improve our understanding of different field sources. The lithospheric magnetic field generated by the magnetized rocks in the lithosphere constitutes an important ingredient of geomagnetic field models (Liu PF et al., 2023). modeling of the lithospheric field help us understand many key issues in Earth science, such as plate tectonics and ocean ridge spreading, and play an important role in some industrial applications, e.g. directional drilling, navigation (Kother et al., 2015; Saltus et al., 2023).

Since the potential of the magnetic field originating from the Earth's interior obeys Laplacian Equation, it is popular to model the lithospheric field in spherical harmonics (Maus, 2010; Sabaka et al., 2020; Wang J et al., 2023). Due to the local feature of lithospheric field and regional distribution of data noise, local basis functions rather than global spherical harmonics are thought to be more suitable (Kother et al., 2015) and widely applied to lithospheric field models (Kother et al., 2015; Olsen et al., 2017; Langlais et al., 2019). One of successful examples is the LCS-1 model derived from CHAMP and *Swarm* satellite observations based on equivalent monopole source method (Olsen et al., 2017). Other approaches with local support include spherical triangle tessellations (Stockmann et al., 2009), (depleted) harmonic splines (Langel and Whaler, 1996), spherical cap harmonics (Haines, 1985; Thébault, 2006), equivalent dipole sources (Mayhew, 1979; von Frese et al., 1981; Covington, 1993; Dyment and Arkani-Hamed, 1998; Langlais et al., 2004, 2019) etc. In this article, we are concerned with the equivalent dipole source

Correspondence to: L. Yin, lyin@must.edu.mo
P. F. Liu, pfliu@must.edu.mo
Received 28 FEB 2025; Accepted 09 APR 2025.
First Published online 24 APR 2025.

method due to that it is related to the magnetization in the lithosphere and thus has more physical meaning.

In equivalent dipole source methods, a spherical grid is needed to discretize the spherical domain of the lithosphere. Due to the singularity and non-uniform grid distribution near the poles, the longitude–latitude grid discretization is usually avoided and several alternative grid techniques, for example, icosahedral mesh and polar coordinate subdivision mesh, are studied in lithospheric field modeling (Covington, 1993; Kother et al., 2015; Langlais et al., 2019). In this study, a new grid technique, namely cubed-sphere grid (Ronchi et al., 1996; Yin L et al., 2017), is employed and an equivalent dipole source method based on such grid is proposed. The employed cubed-sphere grid has advantages of being quasi-uniform and free of singularity, and has been widely applied in numerical simulations of various areas (Yang C et al., 2010; Yin L et al., 2017, 2022, 2023). In addition to grid advantages, the proposed method has capabilities of carrying out both global and regional modeling and combining data with various altitudes. Moreover, local influence of polar noise, easy application of physically meaningful regularization and convenient parallelization are some other benefits we may obtain with the proposed method.

In this paper, we develop a cubed-sphere based method for modeling the lithospheric magnetic field, and derive global and regional models from *Swarm Alpha* satellite and Macau Science Satellite-1 (MSS-1) observations. The remainder of this paper is organized as follows. In Section 2, we present the modeling method including the forward modeling on the cubed-sphere grid and the inversion procedure to estimate the model parameters. In Section 3, we carry out several numerical tests to validate the forward modeling method and the inversion procedure. Then we report the model results based on the realistic magnetic data from *Swarm Alpha* satellite and MSS-1 missions in Section 4. The conclusion is given in Section 5.

2. Modeling Method

2.1 Forward Modeling

According to the potential theory (Blakely, 1996), the magnetic field above the Earth's surface generated by the magnetized materials in the lithosphere can be represented by the gradient of its scalar potential $\boldsymbol{B}(\boldsymbol{r}') = -\nabla' U(\boldsymbol{r}')$, where $\boldsymbol{r}'$ is the position vector of the observation site and ∇' is gradient operator for observation coordinates $\boldsymbol{r}'$. The scalar potential $U(\boldsymbol{r}')$ can be obtained by an integral Equation over entire magnetized domain

$$U(\boldsymbol{r}') = -\frac{\mu_0}{4\pi}\int \boldsymbol{M}(\boldsymbol{r})\cdot\nabla'\frac{1}{|\boldsymbol{r}'-\boldsymbol{r}|}\,\mathrm{d}v = \frac{\mu_0}{4\pi}\int \boldsymbol{M}(\boldsymbol{r})\cdot\frac{\boldsymbol{r}'-\boldsymbol{r}}{|\boldsymbol{r}'-\boldsymbol{r}|^3}\,\mathrm{d}v, \tag{1}$$

where μ_0 is the permeability of free space with value $4\pi\times10^{-7}$ H/m and $\boldsymbol{M}(\boldsymbol{r})$ is the magnetization vector at the position $\boldsymbol{r}$. $|\boldsymbol{r}'-\boldsymbol{r}|$ is the distance between the observation site $\boldsymbol{r}'$ and the magnetization source position $\boldsymbol{r}$. $\mathrm{d}v$ is the differential volume element of the integrated domain. From Equation (1), we can derive the integral formula for the magnetic field

$$\boldsymbol{B}(\boldsymbol{r}') = -\nabla' U(\boldsymbol{r}') = \frac{\mu_0}{4\pi}\int\left(\frac{3\boldsymbol{M}\cdot\boldsymbol{R}}{R^5}\boldsymbol{R}-\frac{\boldsymbol{M}}{R^3}\right)\mathrm{d}v, \tag{2}$$

where $\boldsymbol{R} = \boldsymbol{r}'-\boldsymbol{r}$ and $R = |\boldsymbol{R}|$ is the L_2 norm of $\boldsymbol{R}$.

To calculate the integral, the lithosphere is modeled as a thin spherical shell and discretized by a cubed-sphere grid technique (Yin L et al., 2017). In a cubed-sphere, the spherical surface is divided into six identical patches, by projecting the six faces of an inscribed cube onto the concerned spherical surface. Each patch is governed by a local cubed-sphere coordinate system and the whole spherical surface is analytically described by the composition of six identical coordinate systems. To generate a quasi-uniform mesh, the gnomonic projection introduced by Ronchi et al. (1996) is adopted to form the local coordinate system for each patch. An illustration of the employed cubed-sphere grid is given in Figure 1. By varying the radius of the spherical surface, the cubed-sphere grid can be extended straightforwardly to a three-dimensional spherical shell domain. The local coordinates of three-dimensional cubed-sphere grid are (ξ,η,r), where $\xi,\eta\in[-\pi/4,\pi/4]$ are angular variables determining the location on spherical surface within one patch, and r is the radius of the spherical surface. The transformation relationships between Cartesian coordinates (x,y,z) and the cubed-sphere coordinates (ξ,η,r) are

$$x = \frac{r}{\sqrt{\delta}},\quad y = \frac{r\tan\xi}{\sqrt{\delta}},\quad z = \frac{r\tan\eta}{\sqrt{\delta}}, \tag{3}$$

where $\delta = 1+\tan^2\xi+\tan^2\eta$ is an auxiliary variable. The differential volume element of cubed-sphere coordinates is $\mathrm{d}v = \sqrt{g}\,\mathrm{d}\xi\,\mathrm{d}\eta\,\mathrm{d}r$, where $\sqrt{g} = r^2\sec^2\xi\sec^2\eta/\delta^{\frac{3}{2}}$ (Yin L et al., 2017). For symmetry, the grid numbers in ξ and η directions are set to be same. The total number of grid cells can be expressed by $N_{cs} = N_s\times N_s\times N_r\times 6$, where N_s is grid number in ξ (η) direction and N_r is grid number in r direction. In present study, one layer cubed-sphere grid is concerned, that is to say, $N_r = 1$.

After discretizing the integrated domain by the cubed-sphere grid, the integral (2) over the whole domain equals summation of the individual integrals over each grid cell.

$$\boldsymbol{B}(\boldsymbol{r}') = \frac{\mu_0}{4\pi}\sum_{i=1}^{N_{cs}}\int_i\left(\frac{3\boldsymbol{M}\cdot\boldsymbol{R}}{R^5}\boldsymbol{R}-\frac{\boldsymbol{M}}{R^3}\right)\mathrm{d}v = \sum_{i=1}^{N_{cs}}\boldsymbol{B}_i, \tag{4}$$

where N_{cs} is the total cell number of the cubed-sphere grid and $\boldsymbol{B}_i$ is the contribution from i-th grid cell. Regarding a cubed-sphere

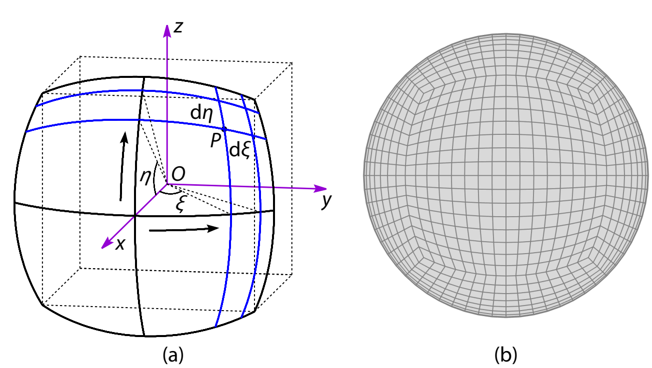

Figure 1. Illustration of the cubed-sphere grid generated by the gnomonic projection. (a) Geometric relationship between the cubed-sphere coordinate system and the Cartesian coordinate system on one patch. (b) An example of generated cubed-sphere grid with coarse spatial resolution.

grid cell, its contribution to the observation magnetic field is recast as

$$\boldsymbol{B}_i = \frac{\mu_0}{4\pi}\int_i\left(\frac{3\boldsymbol{M}\cdot\boldsymbol{R}}{R^2}\boldsymbol{R}-\boldsymbol{M}\right)\frac{\sqrt{g}}{R^3}\,\mathrm{d}\xi\,\mathrm{d}\eta\,\mathrm{d}r. \tag{5}$$

Such integral is difficult to be solved analytically, and is usually calculated approximately by numerical integration methods. Here we employ a second-order linear reconstruction (Moukalled et al., 2016) to obtain an approximate numerical solution. Let ϕ denote the integrated function in Equation (5) and express it in Taylor expansions:

$$\phi = \phi_C + (\boldsymbol{r}-\boldsymbol{r}_C)\cdot(\nabla\phi)_C + O\left(|\boldsymbol{r}-\boldsymbol{r}_C|^2\right), \tag{6}$$

where only linear terms are included and C is the cell centroid. The integral of ϕ over i-th grid cell can be calculated as

$$\int_i \phi\,\mathrm{d}\xi\,\mathrm{d}\eta\,\mathrm{d}r = (\phi_C)_i(\Delta\xi\Delta\eta\Delta r)_i + O\left(|\boldsymbol{r}-\boldsymbol{r}_C|^2\right), \tag{7}$$

where $\Delta\xi, \Delta\eta, \Delta r$ are grid cell sizes. Note that the integral of the second term in Equation (6) vanishes as the coordinates of the centroid C is $\boldsymbol{r}_C = \frac{1}{\Delta\xi\Delta\eta\Delta r}\int \boldsymbol{r}\,\mathrm{d}\xi\,\mathrm{d}\eta\,\mathrm{d}r$ (Yin L et al., 2023). The Equation (7) provides an approximate solution with second-order accuracy to the integral over grid cell, i.e. replacing the integrated function by its constant value at the cell centroid. Therefore, we approximate the integral (5) by

$$\boldsymbol{B}_i = \frac{\mu_0}{4\pi}\left[\left(\frac{3\boldsymbol{M}_C\cdot\boldsymbol{R}_C}{R_C^2}\boldsymbol{R}_C-\boldsymbol{M}_C\right)\frac{\sqrt{g_C}}{R_C^3}\Delta\xi\Delta\eta\Delta r\right]_i, \tag{8}$$

and calculate $\boldsymbol{B}_i$ in Cartesian coordinates as follows

$$\boldsymbol{r}' = (x', y', z'), \quad \boldsymbol{r} = (x, y, z), \tag{9}$$

$$\boldsymbol{R} = (R_x, R_y, R_z) = (x'-x, y'-y, z'-z), \tag{10}$$

$$R = \sqrt{R_x^2+R_y^2+R_z^2}, \tag{11}$$

$$\boldsymbol{M}\cdot\boldsymbol{R} = M_xR_x + M_yR_y + M_zR_z. \tag{12}$$

The field components in spherical coordinate system (r, θ, ϕ) are obtained by

$$B_{r,i} = \boldsymbol{B}_i\cdot\hat{r} = \frac{\mu_0}{4\pi}\left[\left(\frac{3\boldsymbol{M}_C\cdot\boldsymbol{R}_C}{R_C^2}\boldsymbol{R}_C\cdot\hat{r}-\boldsymbol{M}_C\cdot\hat{r}\right)\frac{\sqrt{g_C}}{R_C^3}\Delta\xi\Delta\eta\Delta r\right]_i, \tag{13}$$

$$B_{\theta,i} = \boldsymbol{B}_i\cdot\hat{\theta} = \frac{\mu_0}{4\pi}\left[\left(\frac{3\boldsymbol{M}_C\cdot\boldsymbol{R}_C}{R_C^2}\boldsymbol{R}_C\cdot\hat{\theta}-\boldsymbol{M}_C\cdot\hat{\theta}\right)\frac{\sqrt{g_C}}{R_C^3}\Delta\xi\Delta\eta\Delta r\right]_i, \tag{14}$$

$$B_{\phi,i} = \boldsymbol{B}_i\cdot\hat{\phi} = \frac{\mu_0}{4\pi}\left[\left(\frac{3\boldsymbol{M}_C\cdot\boldsymbol{R}_C}{R_C^2}\boldsymbol{R}_C\cdot\hat{\phi}-\boldsymbol{M}_C\cdot\hat{\phi}\right)\frac{\sqrt{g_C}}{R_C^3}\Delta\xi\Delta\eta\Delta r\right]_i, \tag{15}$$

where $\hat{r}, \hat{\theta}, \hat{\phi}$ are unit base vectors of spherical coordinate system.

The Equation (8) can be rewritten as

$$\boldsymbol{B}_i = \frac{\mu_0}{4\pi}\left[\left(\frac{3\boldsymbol{m}_C\cdot\boldsymbol{R}_C}{R_C^2}\boldsymbol{R}_C-\boldsymbol{m}_C\right)\frac{1}{R_C^3}\right]_i, \quad \boldsymbol{m}_C = \boldsymbol{M}_C\sqrt{g_C}\Delta\xi\Delta\eta\Delta r, \tag{16}$$

which corresponds to the magnetic field generated by a dipole with moment $\boldsymbol{m}_C$ at the centroid C. Actually, the employed linear approximation is identical to the well-known equivalent dipole source method, which is widely applied in the lithospheric field modeling (Mayhew, 1979; von Frese et al., 1981; Covington, 1993; Langlais et al., 2004, 2019). We derive the magnetic field in the integral formulation (5) due to the consideration of future possible extension of high-accuracy integration scheme, such as Gauss-Legendre quadrature method (Du J et al., 2015).

2.2 Inversion Method

In the inversion process, the direction of magnetization vector is fixed and is set to be as same as a priori value, i.e. $\boldsymbol{M} = \lambda\boldsymbol{M}_0$, where $\boldsymbol{M}_0$ is a priori reference magnetization and λ is the inversion parameter. The magnetic field at observation site is then recast as

$$B_e = \frac{\mu_0}{4\pi}\sum_{i=1}^{N_{cs}}\left[\left(\frac{3\boldsymbol{M}_0\cdot\boldsymbol{R}_C}{R_C^2}\boldsymbol{R}_C\cdot\hat{e}-\boldsymbol{M}_0\cdot\hat{e}\right)\frac{\lambda\sqrt{g_C}}{R_C^3}\Delta\xi\Delta\eta\Delta r\right]_i, \tag{17}$$

where $\hat{e}$ denotes $\hat{r}, \hat{\theta}$ or $\hat{\phi}$. The forward calculation Equation (17) can be written in a matrix form:

$$\boldsymbol{B}_e = \boldsymbol{G}_e\boldsymbol{m}, \tag{18}$$

where $\boldsymbol{B}_e$ is a column vector containing model predictions of e component, $\boldsymbol{m} = [\lambda_1, \lambda_2, \ldots, \lambda_{N_{cs}}]^{\mathrm{T}}$ is the model vector, $\boldsymbol{G}_e$ is the corresponding matrix which can be derived from Equation (17).

The inversion objective function is constructed as

$$\phi(\boldsymbol{m}) = \phi_d + \beta\phi_m, \tag{19}$$

where ϕ_d is the data fitting residual function, ϕ_m is the model objective function, and β is a regularization parameter. The data fitting residual function is defined as

$$\phi_d = \sum_{k=1}^{K}\gamma_k\sum_{j=1}^{N_k}\left(\frac{d_{k,j}^p - d_{k,j}^o}{\varepsilon_{k,j}}\right)^2, \tag{20}$$

where K is the number of data kind, γ_k is the weight of k-th kind data, N_k is the number of k-th kind data, $d_{k,j}^p$ and $d_{k,j}^o$ are model prediction and observation value of j-th point of k-th kind data, respectively, and $\varepsilon_{k,j}$ is the weight of j-th data residual of k-th kind data. The model objective function is defined as

$$\phi_m = \sum_{i=1}^{N_{cs}}\omega_i(m_i - m_i^{\mathrm{ref}})^2, \tag{21}$$

where ω_i is the weight of i-th model residual, m_i is i-th model element, and m_i^{ref} is i-th element of reference model $\boldsymbol{m}^{\mathrm{ref}}$. Rewritting the Equations (20) and (21) into the matrix form, the inversion objective function is updated by

$$\phi(\boldsymbol{m}) = \sum_{k=1}^{K}\gamma_k||\boldsymbol{W}_{d,k}(\boldsymbol{d}_k^p - \boldsymbol{d}_k^o)||_2^2 + \beta||\boldsymbol{W}_m(\boldsymbol{m}-\boldsymbol{m}^{\mathrm{ref}})||_2^2, \tag{22}$$

where $\boldsymbol{W}_{d,k} = \mathrm{diag}(1/\varepsilon_{k,j})$, $\boldsymbol{W}_m = \mathrm{diag}(\sqrt{\omega_i})$ are the diagonal weight matrices. To find the minimum of the inversion objective function $\phi(\boldsymbol{m})$, take the partial derivative of $\boldsymbol{m}$ for the Equation (22) and set $\partial\phi(\boldsymbol{m})/\partial\boldsymbol{m} = 0$, resulting in the following linear algebraic system:

$$\boldsymbol{A}\boldsymbol{m} = \boldsymbol{b}, \tag{23}$$

$$\boldsymbol{A} = \sum_{k=1}^{K}\gamma_k\boldsymbol{G}_k^{\mathrm{T}}\boldsymbol{W}_{d,k}^{\mathrm{T}}\boldsymbol{W}_{d,k}\boldsymbol{G}_k + \beta\boldsymbol{W}_m^{\mathrm{T}}\boldsymbol{W}_m, \tag{24}$$

$$\boldsymbol{b} = \sum_{k=1}^{K} \gamma_k \boldsymbol{G}_k^{\mathrm{T}} \boldsymbol{W}_{d,k}^{\mathrm{T}} \boldsymbol{W}_{d,k} \boldsymbol{d}_k^{o} + \beta \boldsymbol{W}_m^{\mathrm{T}} \boldsymbol{W}_m \boldsymbol{m}^{\mathrm{ref}}. \tag{25}$$

The above linear algebraic system is solved by a direct solver (LU decomposition) in MATLAB and the regularization parameter β is determined by the L-curve method (Lawson and Hanson, 1995). Uniform weights are employed for data fitting residual function (20) and model objective function (21) in present study.

3. Method Validation

3.1 Forward Modeling Method

In forward modeling, we calculate the magnetic field above the surface according to a given magnetization distribution. The validation of the proposed forward modeling method can be performed by the aid of the Runcorn's theorem (Runcorn, 1975a, b), a well-known annihilator of lithospheric magnetic effect. The Runcorn's theorem states a special phenomenon that a spherical shell with uniform thickness and susceptibility magnetized by an internal dipole field produces no magnetic field outside. This phenomenon was successfully applied to explain the natural remanent magnetization of the lunar crust (Runcorn, 1975a) and was usually used as an analytical solution to validate the accuracy of the forward modeling method (Baykiev et al., 2016; Langlais et al., 2019). Here we follow this approach to test our code.

To resemble the Earth's lithosphere, a spherical shell with 26.5 km thickness, which is an average thickness of global magnetized lithosphere (Du JS et al., 2015), and uniform susceptibility of 0.1 SI is adopted in present test. The shell's outer radius is set to 6371.2 km, the radius of the Earth's magnetic reference sphere. The magnetic moment of the internal dipole is set to be 7.94×10^{22} A·m^2, which is a typical value of the Earth's dipole moment (Baykiev et al., 2016). The corresponding root-mean-squared (rms) magnetization is 3.48 A/m. We calculate the magnetic field at satellite altitude (400 km) in a 1° longitude–latitude grid produced by the spherical shell discretized with four different spatial resolutions ($N_s = 48, 64, 72, 96$) respectively. The grid numbers of the spherical shell are respectively 13,824, 24,576, 31,104, 55,296 and the rms grid lengths are respectively $191.7, 143.8, 127.8, 95.8$ km. The numerical result can directly reflect the discretization error, since it should be zero field in ideal situation. Figure 2 shows the radial components of the magnetic field at 400 km altitude for the four different grids. It is observed that the radial magnetic field is zero almost everywhere except in eight small regions which correspond to the eight discontinuous vertices of the cubed-sphere grid. The maximum value is nearly 1 nT (precisely speaking 1.07 nT) for $N_s = 48$ and much smaller than 1 nT for other three grids, and decreases as the spatial resolution increases. The convergence result for L_1, L_2 and L_∞ norms of the radial magnetic field at 400 km altitude is given in Figure 3. From Figure 3, second-order convergence rates can be observed for L_1, L_2 and L_∞ norms, validating the accuracy of the proposed forward modeling method.

In lithospheric models based on equivalent source inversion method, the grid technique used to discretize spherical surface usually plays an important role in terms of the accuracy (Covington, 1993; Kother et al., 2015; Langlais et al., 2019). In Langlais et al. (2019), the icosahedral and polar subdivision meshes were tested by the aid of the Runcorn's theorem and a model of the crustal magnetic field of Mars was successfully built based on the

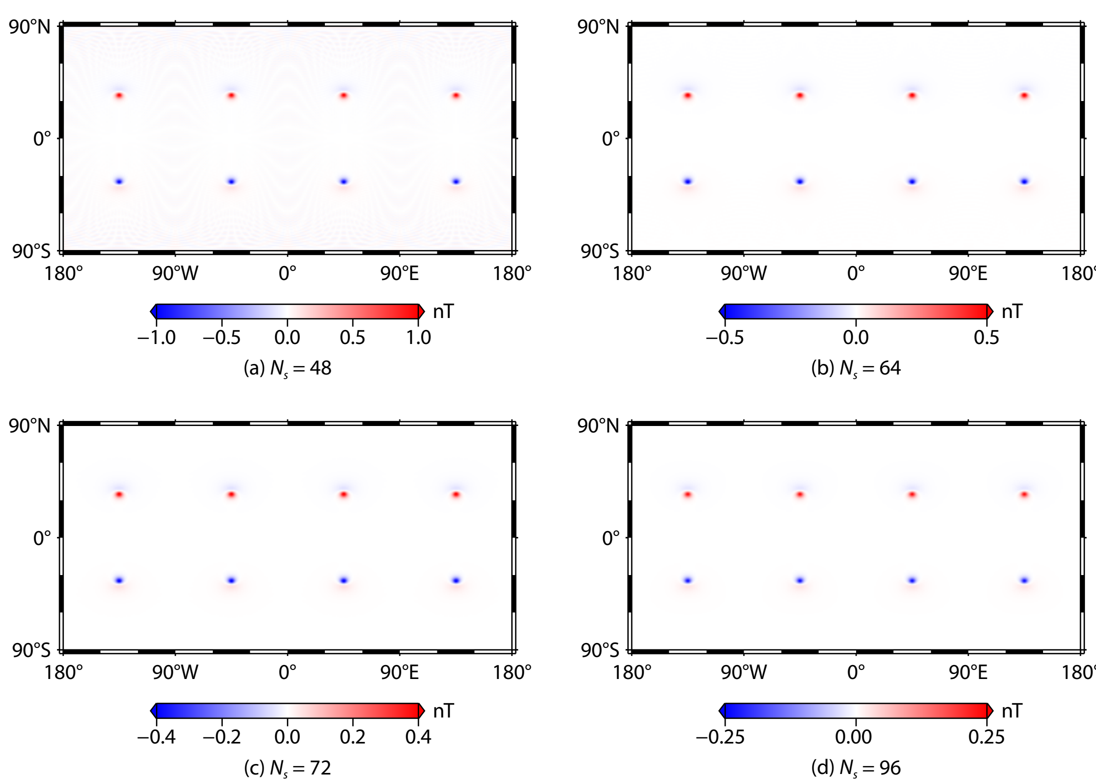

Figure 2. Radial components of the magnetic field at 400 km altitude for the four different grids of the spherical shell.

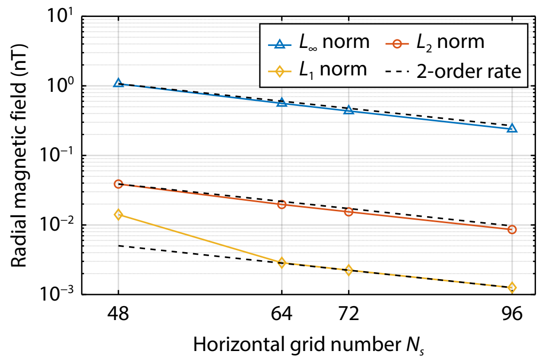

Figure 3. Convergence result for L_1, L_2 and L_∞ norms of the radial magnetic field at 400 km altitude.

latter mesh. For the purpose of comparison with the above two kinds of mesh, we calculate the same case using our code. Following Langlais et al. (2019), the outer radius of the spherical shell is set to 3393.5 km (the mean radius of Mars) and the thickness is 40 km. The magnetic moment of the centered axial dipole is set according to the condition that the magnetization equals to 1 A/m at the equator. Choosing N_s = 46, the number of grid cells is 12,696, comparable (slightly less) to the dipole numbers (12,962 and 12,922) used in Langlais et al. (2019, Appendix A). Regarding spatial resolution, the corresponding maximum grid length is 115.2 km and the rms grid length is 106.1 km, both smaller than the mean resolution of 119.5 km in Langlais et al. (2019, Appendix A). The input rms magnetization is 1.44 A/m in the employed cubed-sphere grid. The magnetic field at an altitude of 150 km is calculated in a 1° longitude–latitude grid and Figure 4 shows the resulting radial component whose amplitude varys from −3.2 nT to 3.2 nT. From the figure we observe that the radial magnetic field is very close to 0, the ideal value, for the whole surface. The maximun intensity is just around 3 nT, smaller than 10 nT in Langlais et al. (2019, Appendix A) and occurs only in eight very small regions. The mean absolute value of the radial magnetic field is only 0.27 nT in our cubed-sphere grid, much smaller than the icosahedral and polar subdivision meshes (2.25 nT and 1.36 nT) in Langlais et al. (2019, Appendix A). As far as the maximum intensity and the mean absolute value are concerned, the cubed-sphere grid employed in present study shows considerable

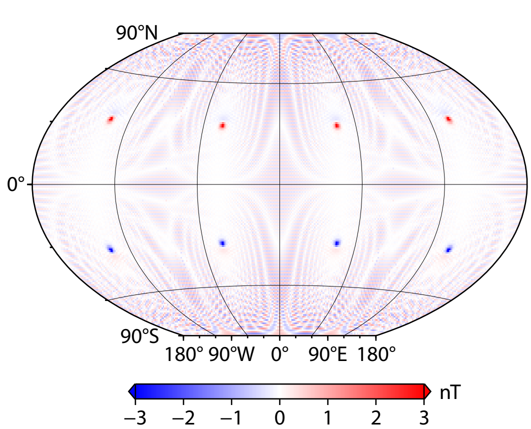

Figure 4. Radial component of the magnetic field at an altitude of 150 km.

advantages over the icosahedral and polar subdivision meshes.

Another case that can be used to test the forward modeling code is the vertically integrated magnetization (VIM) model (Gubbins et al., 2011; Du JS et al., 2015), which involves a global lithospheric magnetization model related to geological information. Here we use a global lithospheric magnetization model same to that in Du JS et al. (2015), constructed by combining the induced magnetization model of Hemant and Maus (2005) and the oceanic remanent magnetization model of Masterton et al. (2013). The model was used in Du JS et al. (2015) to test the Gauss–Legendre quadrature integration method based on spherical coordinate system. To further validate our forward modeling code, we compute the magnetization on the cubed-sphere grid by interpolation from the global lithospheric magnetization model and calculate the corresponding magnetic field at satellite altitude (400 km). The calculation results are compared with the high-accuracy solutions obtained by the Gauss–Legendre quadrature integration method developed in Du JS et al. (2015). The spherical shell with thickness of 26.5 km and outer radius of 6371.2 km is discretized by 98,304 grid cells (N_s = 128). In Figure 5, we display the three components of magnetic field at 400 km altitude calculated by the proposed method and their differences with Gauss–Legendre quadrature solution. From Figure 5 we observe that the results by present method and Gauss–Legendre quadrature integration method agree well. The errors of the magnetic components are below 1 nT almost everywhere and the relationship between the errors and the eight discontinuous vertices, which is obvious in annihilator tests based on Runcorn's theorem, is no more observed. Such observation further confirms the correctness and advantage of the proposed forward modeling method based on the cubed-sphere grid.

3.2 Inversion Method

In this section, we test the inversion method by the synthetic data based on the CHAOS-7 model (Finlay et al., 2020). The crustal magnetic field up to degree 110 extracted from the CHAOS-7 model is added by random Gauss noises with a multiplier α to generate the final synthetic data. Only radial component of the crustal field is adopted for simplicity and the model result is generated on a 1° longitude–latitude grid at an altitude 400 km, yielding 64,800 data in total. The thickness and outer radius of the spherical shell are respectively 26.5 km and 6371.2 km, following the VIM model test in Section 3.1. The shell is discretized by the cubed-sphere grid with resolution N_s = 48 (13,824 grid cells), and the number of λ parameters is therefore 13,824. The VIM model introduced in Section 3.1 is used as the reference magnetization $\boldsymbol{M}_0$ and the reference $\lambda(\boldsymbol{m}^{\text{ref}})$ is set to zero.

The values of model parameter λ are estimated from the synthetic data with four different regularization parameters β = 0, 0.1, 1, 10. Three types of input synthetic data with varied multiplier α are examined, of which two are obtained with α = 0, 0.2 respectively. The third type data is generated by adding Gauss noise with α = 0.5 in polar regions, where latitude is greater than 55° or less than −55°, and α = 0.2 in other region. The rms misfit values of inversion results are listed in Table 1. From the table it is observed that all the inversion cases succeed with low rms misfit values,

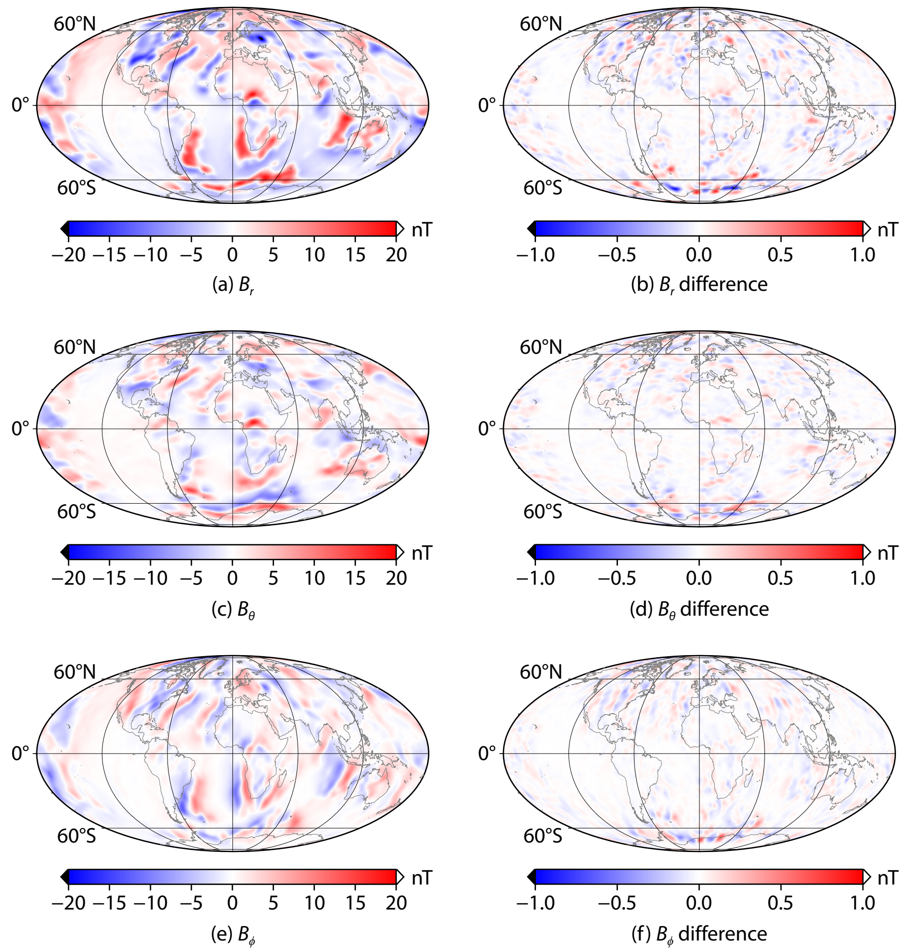

Figure 5. Three components of the magnetic field at 400 km altitude calculated by the proposed method and their differences with the high-accuracy solutions calculated by the Gauss–Legendre quadrature integration method developed in Du JS et al. (2015).

Table 1. The rms misfit values (in nT) of inversion results for three data types with four different regularization parameters β = 0, 0.1, 1, 10.[a]

Data type	Multiplier α	β = 0	β = 0.1	β = 1	β = 10
1	0	0.022	0.034	0.086	0.263
2	0.2	0.483	0.488	0.502	0.568
3	0.2, 0.5	1.017	1.020	1.030	1.071

[a]Data type 1 is the noise-free synthetic data (Gauss noise is multiplied by α = 0). Data type 2 is the synthetic data with multiplier α = 0.2. Data type 3 is generated by adding Gauss noise with multiplier α = 0.5 in polar region, where latitude is greater than 55° or less than −55°, and multiplier α = 0.2 in other region. Only radial magnetic data is involved here.

including the models with no regularization (β = 0). As expected, the rms misfit value becomes larger as the multiplier of Gauss noise increases. Besides, the rises of regularization parameter β enlarge the rms misfit as well. To obtain a best reasonable model, a careful choice of β might be required. The misfit results also indicate that the grid resolution N_s = 48 is a suitable choice for the data at satellite altitude (400 km).

According to the estimated model parameter λ, the magnetic field at 400 km altitude is reconstructed and compared to the initial crustal field of the CHAOS-7 model. Figure 6 shows the residuals between reconstructed radial magnetic field and the initial data from the CHAOS-7 model. From noise-free (α = 0) cases, we can clearly observe the discrepancies introduced by the regularization. Too large regularization parameter β could bring in significant discrepancy with the initial data and should be avoided as far as possible. Regarding the data type 2 with Gauss noise of α = 0.2, we find that the discrepancy of the regularization-free (β = 0) case grows significantly compared to the noise-free data, and the regularization could help suppress the discrepancy. The lower residuals than the regularization-free case are obtained by β = 0.1 and β = 1, of which the latter seems a little better. No improvement of discrepancy is observed from the β = 10 case. The data type 3 with non-uniform Gauss noise is designed to verify local feature of the employed method. In a model based on local methods, the data in a region with larger noise do not affect the model result in other region, in contrast to the popular spherical harmonic method with global nature. The local feature would

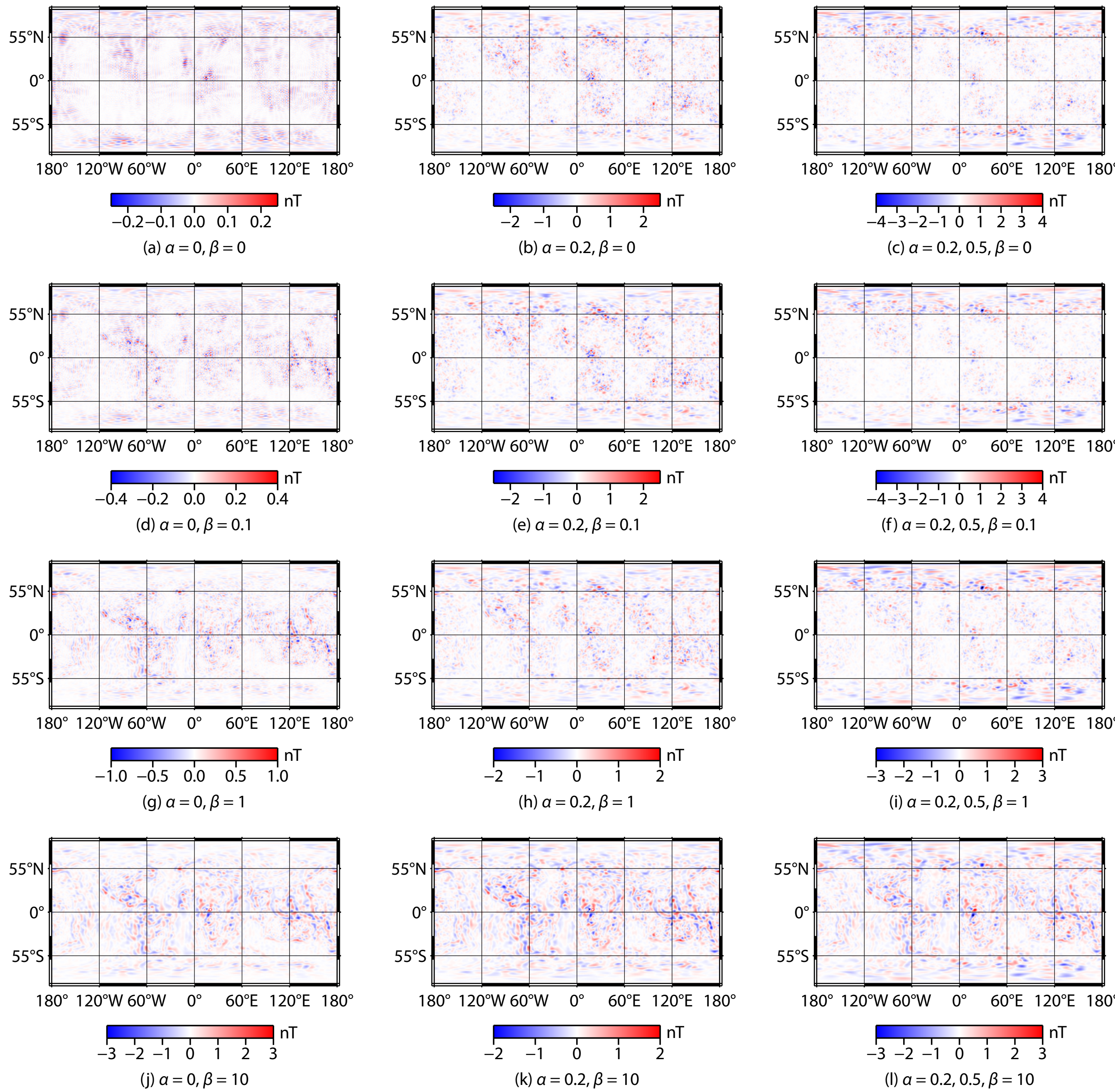

Figure 6. Differences between reconstructed radial magnetic fields according to the estimated models and the initial crustal field of the CHAOS-7 model.

be helpful considering the noise of realistic satellite data in polar regions is usually larger due to the influence of space current systems. From the last column of Figure 6, the local feature of the employed method can be obviously observed. The spatial distributions of residuals show a clear relationship with the distribution of Gauss noise for $\beta = 0, 0.1, 1$ cases. In the $\beta = 10$ case, local feature is masked by the global residual introduced by excessive regularization, implying the regularization parameter 10 is too large in present test.

In summary, the correctness and accuracy of the proposed inversion method are validated by the synthetic data based on the CHAOS-7 model. Although the model with no regularization can be obtained successfully, the proposed regularization with an appropriate parameter could help suppress the model error when inversion data contains noise. On the other hand, some a priori information can be added to the model by appropriate regularization to reduce the inversion nonuniqueness and generate more physically meaningful models instead of purely data-fitting models. This topic, however, is beyond the scope of current paper.

4. Models from Satellite Data

In this section, we build global and regional models by the proposed method using the realistic satellite data from the *Swarm* and MSS-1 missions. The latest magnetic data of MSS-1 observation (from 2023/11/02 to 2024/12/31) and *Swarm Alpha* satellite data in the past three years (from 2022 to 2024) are used in present study. To carry out lithospheric modeling in a sequential approach, special data processing is required to extract lithospheric contributions from original data, which is performed in an ordinary way here. The processing includes data selection according to low Earth's magnetic activity, correction for contributions from other field sources, high-pass filtering along the satellite orbit etc. The details of data processing can be found in Zhang P et al. (2025). Only vertical component of the vector data is involved in the current models and the total data quantities from MSS-1 and *Swarm* missions are 224,022, 420,424 respectively. The models are built based on the cubed-sphere grids with different resolutions and the regularization parameters determined by L-curve method are all found to be $\beta = 1$ in the following models.

4.1 Lat41 Models

It could be helpful to validate the data consistency between the well-known *Swarm* mission and the new MSS-1 mission in terms of lithospheric modeling. With a low inclination of 41°, MSS-1 does not have a global data coverage and comparison in a global scale is not practical. For the purpose of data consistency validation, two models in the region with MSS-1 data coverage (within ±41° latitude), namely Lat41 models, are constructed using only MSS-1 and *Swarm* data respectively. Due to the local feature of the proposed method, it is straightforward to build lithospheric models in any partial region of interest, such as the present Lat41 models. The amount of selected *Swarm* data in the involved region within ±41° latitude is 258,862, comparable to data volume of MSS-1. The parameter numbers in two models using respectively MSS-1 data and *Swarm* data are both 13,824 corresponding to the cubed-sphere grid of $N_s = 48$. The rms misfit values of the two models at $\beta = 1$ are 0.50 (MSS-1 data), 0.61 (*Swarm* data) nT respectively. Figure 7 presents the L-curves of the two Lat41 models, in which the optimal regularization parameters are found to be $\beta = 1$.

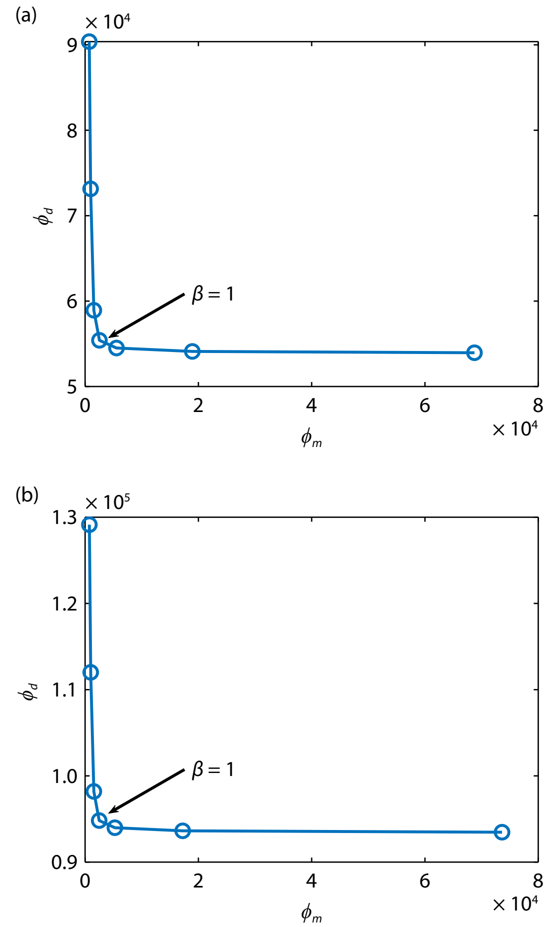

Figure 7. L-curves of the two Lat41 models. (a) Lat41 model using MSS-1 data. (b) Lat41 model using *Swarm* data.

The predicted radial magnetic field of the MSS-1 based model at an altitude of 400 km is presented in Figure 8. It is obvious that the MSS-1 data with the coverage of ±41° latitude affects only the model predicted field corresponding to the same region, as expected. The model predicted field outside the data coverage is determined by the adopted regularization, which is minimization of L_2 norm of the model parameter here. The comparison of predicted radial magnetic field between the two models that use MSS-1 data and *Swarm* data is shown in Figure 9. From the figure, very good agreement can be observed for the two models with the residual below 2 nT, indicating strong data consistency of MSS-1 mission and *Swarm* mission.

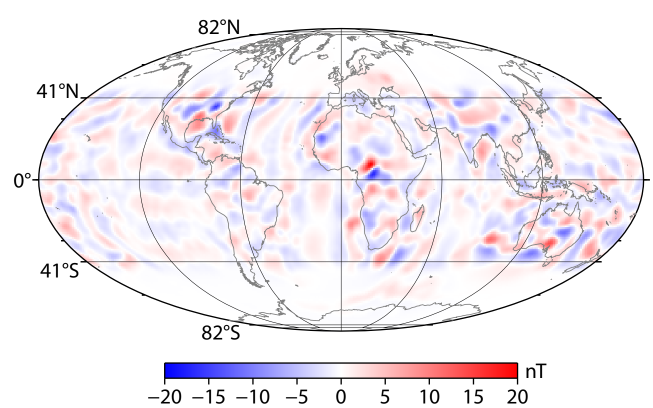

Figure 8. Predicted radial magnetic field of the model using MSS-1 data at an altitude of 400 km.

4.2 Global Models

It is popular to form global lithospheric field models based on satellite data, which is the main concern of this subsection. On the cubed-sphere grid of $N_s = 48$, a global model using 420,424 *Swarm* data and 224,022 MSS-1 data (model SM) is built and compared to a global model based only on *Swarm* data (model S). The predicted radial magnetic field at 400 km altitude from model SM and its residual field after subtracting the predicted field from model S are shown in Figure 10, in which the comparison to the LCS-1 model (Olsen et al., 2017) with degree from 16 to 110 is presented as well. From the residual field distribution in Figure 10b, we observe the expected local effect of MSS-1 data and very good data consistency of *Swarm* and MSS-1 missions. Comparing the predicted fields of model SM and LCS-1 model (Figures 10a and 10c), quite similar spatial distribution in terms of field structure and amplitude can be observed. Large discrepancies mainly locate at the polar regions (see Figure 10d), where special treatment is usually required due to the influence of space currents.

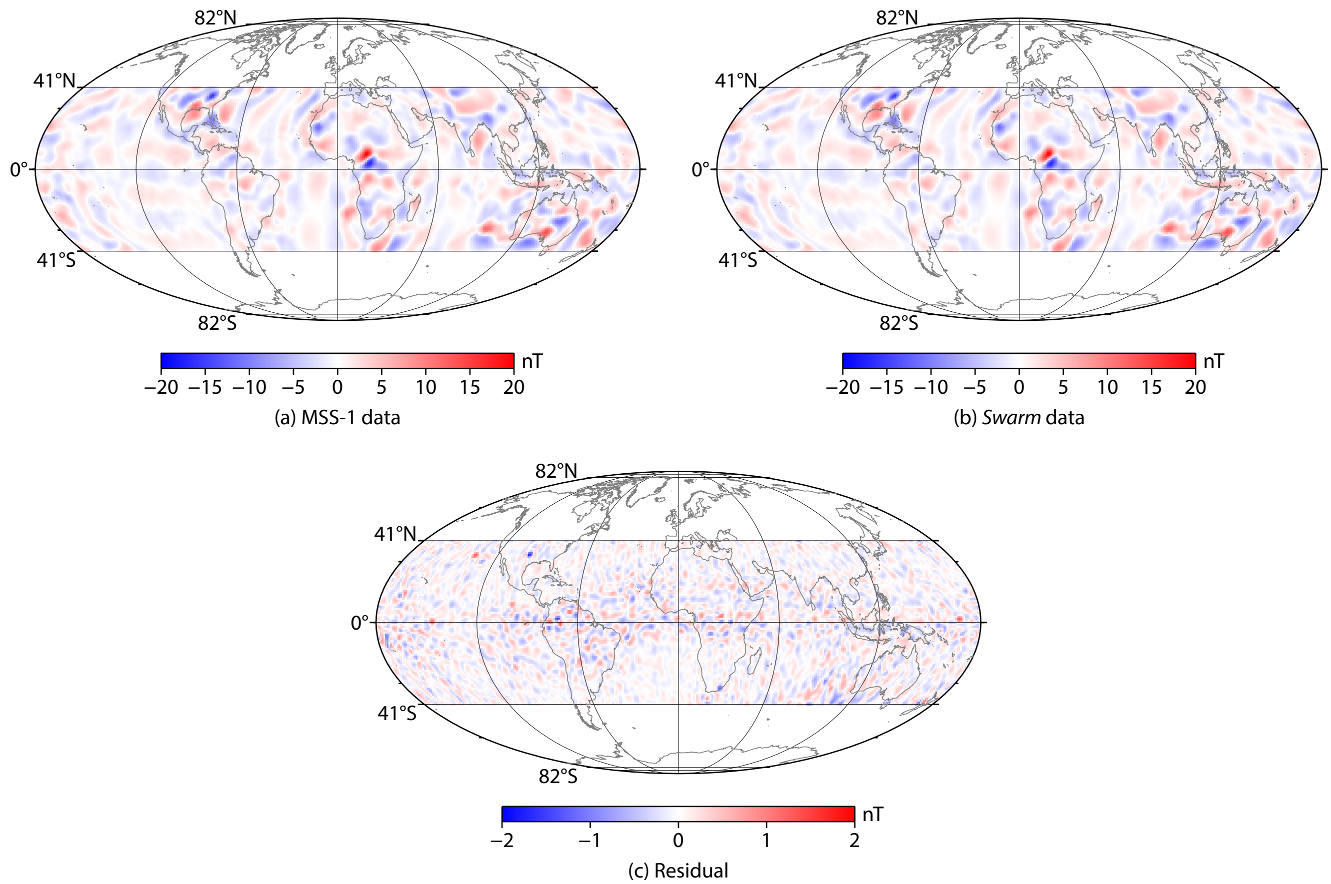

Figure 9. Comparison of predicted radial magnetic field between the two models using MSS-1 data and *Swarm* data. (a) Predicted radial magnetic field by the model using MSS-1 data. (b) Predicted radial magnetic field by the model using *Swarm* data. (c) Residual of predicted radial magnetic field of the two models.

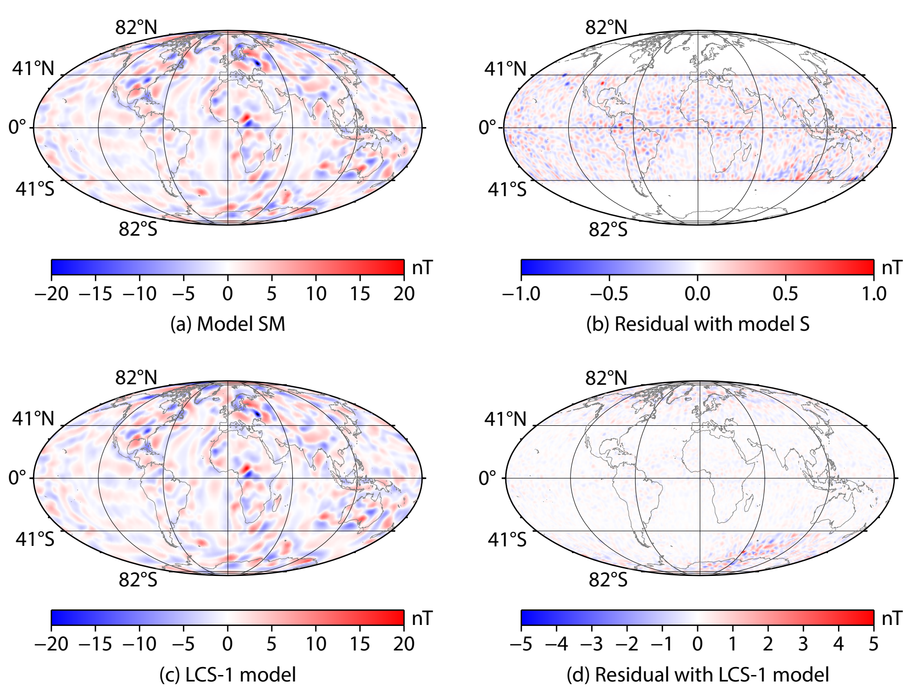

Figure 10. Predicted results and comparisons of the model SM. (a) Predicted radial magnetic field from model SM at an altitude of 400 km. (b) Residual after subtracting the predicted field from model S. (c) Predicted field from the LCS-1 model. (d) Residual after subtracting the predicted field from the LCS-1 model.

The agreement with the LCS-1 model confirms the effectiveness of the proposed method for the realistic satellite data. The discrepancies may come from many aspects, such as inversion data set, weights, regularization etc. To obtain a more accurate and reliable model, more efforts in these aspects are needed and will be made in our following work.

4.3 Regional Models for Africa

One outstanding advantage of the proposed method is the straightforward support for regional modeling. In this subsection, we focus on the application of our method to the construction of regional models. The region involved is a rectangular area with longitude in $[-25°, 55°]$ and latitude in $[-40°, 40°]$, encompassing the African continent. Such region is wholly covered by MSS-1 mission and the model based merely on MSS-1 data can be constructed. To obtain the corresponding regional grid, a cubed-sphere grid of $N_s = 96$ is initially formed and the grid cells outside the region are then discarded, resulting in 7896 inversion parameters. Figure 11 illustrates the grid selection scheme by the region constraint and the resulting regional grid used in the modeling. The initial satellite data is also filtered by the region constraint, resulting in 41,171 MSS-1 data and 55,253 *Swarm* data.

Three models, namely model A, B, C, using respectively MSS-1 data, *Swarm* data, and combined data are successfully built with all rms misfits being around 0.5 nT. Figure 12 shows the predicted radial magnetic field at 400 km altitude from model A and B together with their difference. Again, strong data consistency between MSS-1 and *Swarm* is observed. Figure 13 presents the vector components of the predicted magnetic field from model C at 400 km altitude and comparison results with the LCS-1 model. From the figure good agreements of the three magnetic components can be observed in this regional problem except minor edge effects.

5. Conclusions

A new cubed-sphere based method is developed for global and regional modeling of the lithospheric magnetic field. The proposed method includes a forward model based on the magnetization and a second-order accurate integration scheme, identical to equivalent dipole sources, and a parameter inversion procedure by a least-squares approach combined with a minimum model

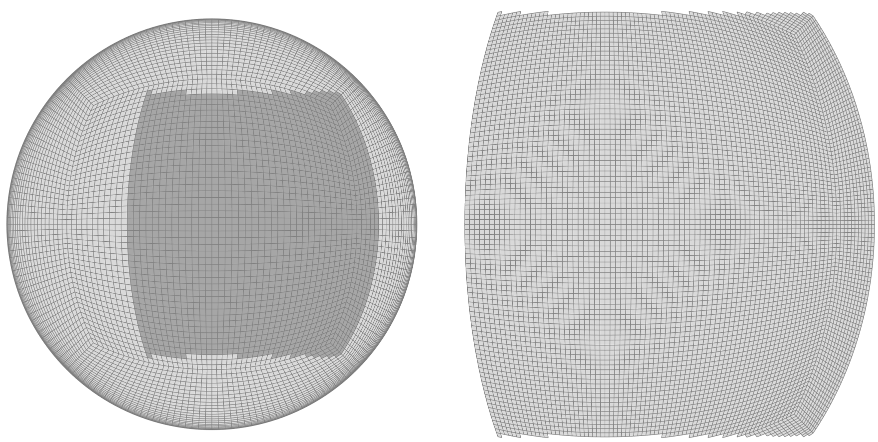

Figure 11. Grid generation in regional modeling of the African continent. (a) Illustration of grid selection scheme by region constraint in a coarser resolution. (b) The final generated grid used in the modeling.

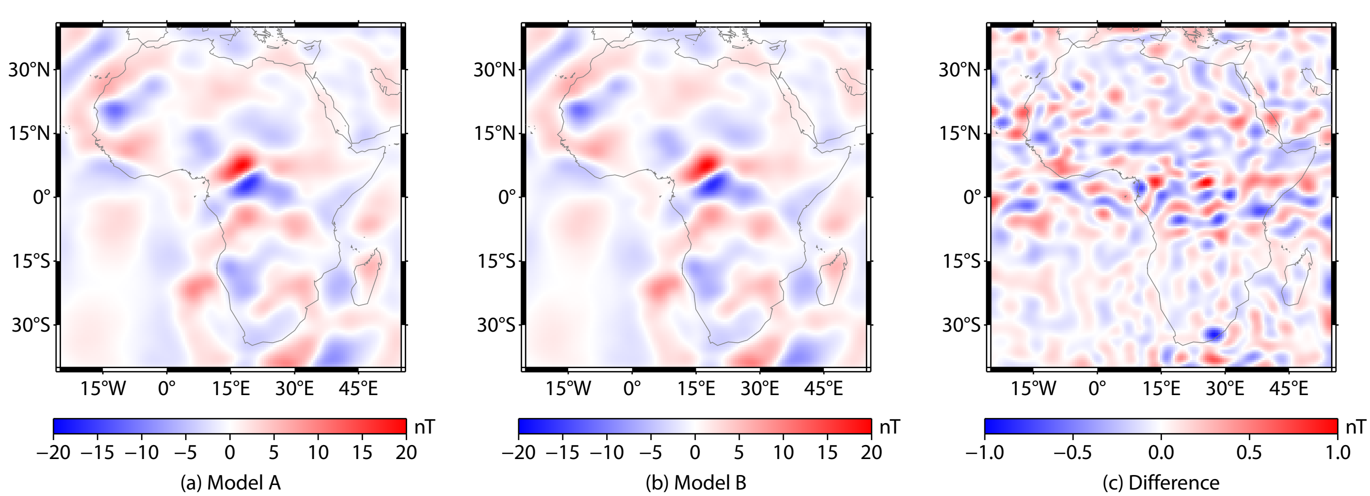

Figure 12. Predicted radial magnetic field at 400 km altitude from model A and B together with their difference.

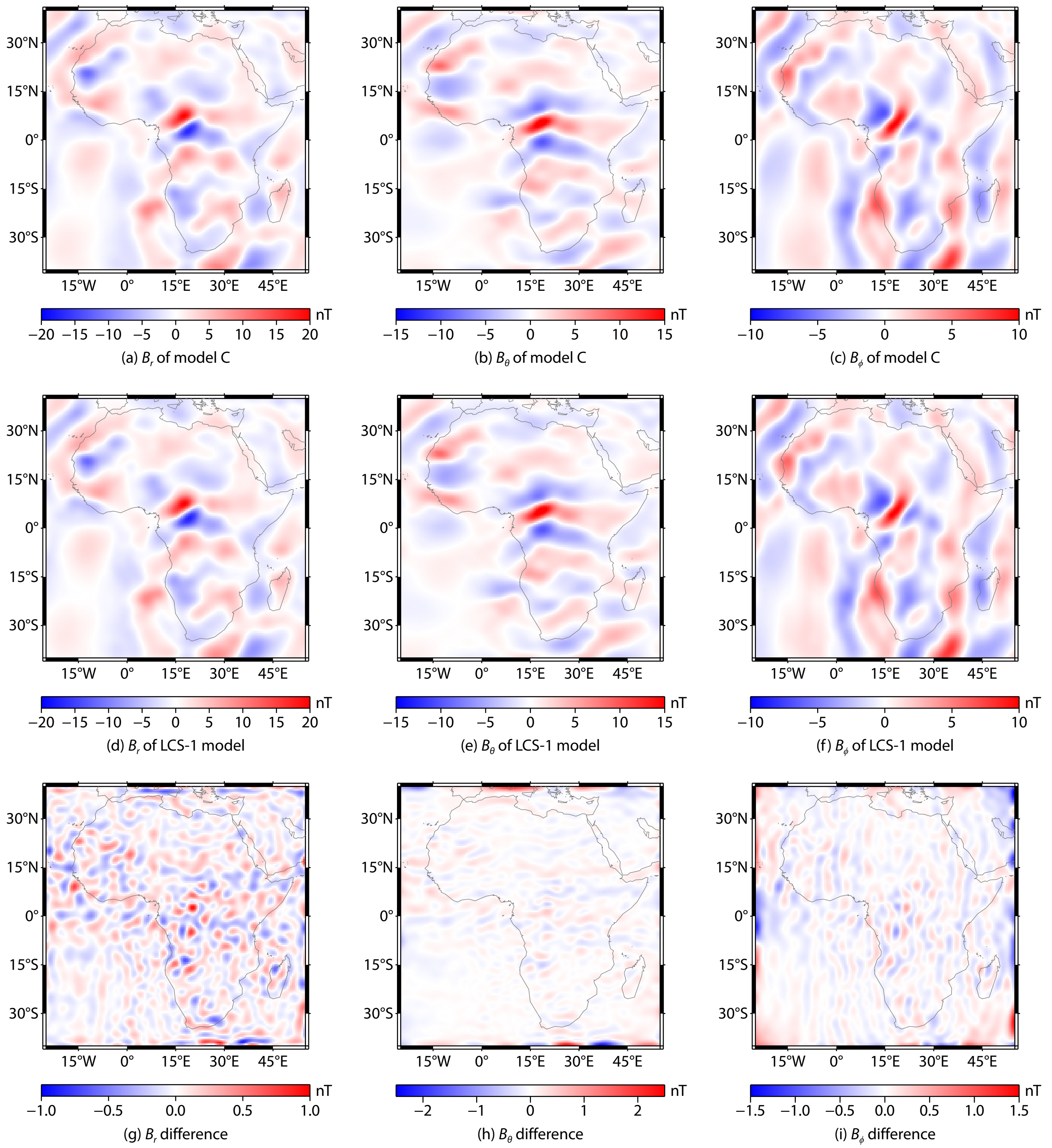

Figure 13. Vector components of the predicted magnetic field at 400 km altitude from model C and the LCS-1 model together with their differences.

regularization. The forward calculation is adequately validated by two annihilator cases according to the Runcorn's theorem and a VIM model constructed by a priori geological information. Several tests of the inversion procedure are carried out by using the synthetic data at satellite altitude based on the CHAOS-7 model, verifying the correctness and accuracy of the inversion method. Based on the latest data from MSS-1 magnetic observation (over one-year) and *Swarm Alpha* satellite (past three years), lithospheric field models in global and regional scale are successfully built by the proposed method, showing good agreement with the LCS-1 model. Meanwhile, data consistency of the two geomagnetic satellite missions in terms of lithospheric modeling and local feature of the proposed method are confirmed according to the model results. To obtain a more accurate and reliable lithospheric model, extra efforts regarding more data involvement, especially gradient data and near surface data, and more physically meaningful regularization are required and planned to be made in our following study.

Acknowledgements

This work is supported by the National Natural Science Foundation of China (42250101, 42250102, 42250103, 12250013) and the Macao Foundation. The MSS-1 magnetic data are available at https://mss.must.edu.mo/data.html. The *Swarm* magnetic data are available at https://swarm-diss.eo.esa.int. We acknowledge Professor Keke Zhang for insightful discussions during the preparation of this paper. We would like to express our appreciation to the anonymous reviewers for their constructive comments.

References

Baykiev, E., Ebbing, J., Brönner, M., and Fabian, K. (2016). Forward modeling magnetic fields of induced and remanent magnetization in the lithosphere using tesseroids. *Comput. Geosci.*, *96*, 124–135. https://doi.org/10.1016/j.cageo.2016.08.004

Blakely, R. J. (1996). *Potential Theory in Gravity and Magnetic Applications*. Cambridge: Cambridge University Press.

Covington, J. (1993). Improvement of equivalent source inversion technique with a more symmetric dipole distribution model. *Phys. Earth Planet. Inter.*, *76*(3-4), 199–208. https://doi.org/10.1016/0031-9201(93)90012-X

Du, J. S., Chen, C., Lesur, V., Lane, R., and Wang, H. L. (2015). Magnetic potential, vector and gradient tensor fields of a tesseroid in a geocentric spherical coordinate system. *Geophys. J. Int.*, *201*(3), 1977–2007. https://doi.org/10.1093/gji/ggv123

Dyment, J., and Arkani-Hamed, J. (1998). Equivalent source magnetic dipoles revisited. *Geophys. Res. Lett.*, *25*(11), 2003–2006. https://doi.org/10.1029/98GL51331

Finlay, C. C., Kloss, C., Olsen, N., Hammer, M. D., Tøffner-Clausen, L., Grayver, A., and Kuvshinov, A. (2020). The CHAOS-7 geomagnetic field model and observed changes in the South Atlantic anomaly. *Earth Planets Space*, *72*(1), 156. https://doi.org/10.1186/s40623-020-01252-9

Gubbins, D., Ivers, D., Masterton, S. M., and Winch, D. E. (2011). Analysis of lithospheric magnetization in vector spherical harmonics. *Geophys. J. Int.*, *187*(1), 99–117. https://doi.org/10.1111/j.1365-246X.2011.05153.x

Haines, G. V. (1985). Spherical cap harmonic analysis. *J. Geophys. Res.: Solid Earth*, *90*(B3), 2583–2591. https://doi.org/10.1029/JB090iB03p02583

Hemant, K., and Maus, S. (2005). Geological modeling of the new champ magnetic anomaly maps using a geographical information system technique. *J. Geophys. Res.: Solid Earth*, *110*(B12), B12103. https://doi.org/10.1029/2005JB003837

Kother, L., Hammer, M. D., Finlay, C. C., and Olsen, N. (2015). An equivalent source method for modelling the global lithospheric magnetic field. *Geophys. J. Int.*, *203*(1), 553–566. https://doi.org/10.1093/gji/ggv317

Langel, R. A., and Whaler, K. A. (1996). Maps of the magnetic anomaly field at Earth's surface from scalar satellite data. *Geophys. Res. Lett.*, *23*(1), 41–44. https://doi.org/10.1029/95GL03092

Langlais, B., Purucker, M., and Mandea, M. (2004). Crustal magnetic field of Mars. *J. Geophys. Res.: Planets*, *109*(E2), E02008. https://doi.org/10.1029/2003JE002048

Langlais, B., Thébault, E., Houliez, A., Purucker, M. E., and Lillis, R. J. (2019). A new model of the crustal magnetic field of Mars using mgs and maven. *J. Geophys. Res.: Planets*, *124*(6), 1542–1569. https://doi.org/10.1029/2018JE005854

Lawson, C. L., and Hanson, R. J. (1995). *Solving Least Squares Problems*. Philadelphia: SIAM.

Liu, P. F., Jiang, Y., Yan, Q., and Hirt, A. M. (2023). The behavior of a lithospheric magnetization and magnetic field model. *Earth Planet. Phys.*, *7*(1), 66–73. https://doi.org/10.26464/epp2023025

Masterton, S. M., Gubbins, D., Müller, R. D., and Singh, K. H. (2013). Forward modelling of oceanic lithospheric magnetization. *Geophys. J. Int.*, *192*(3), 951–962. https://doi.org/10.1093/gji/ggs063

Maus, S. (2010). An ellipsoidal harmonic representation of Earth's lithospheric magnetic field to degree and order 720. *Geochem. Geophys. Geosyst.*, *11*(6), Q06015. https://doi.org/10.1029/2010GC003026

Mayhew, M. A. (1979). Inversion of satellite magnetic anomaly data. *J. Geophys.*, *45*(1), 119–128.

Moukalled, F., Mangani, L., and Darwish, M. (2016). *The Finite Volume Method in Computational Fluid Dynamics: An Advanced Introduction with openFOAM® and Matlab*. Cham: Springer, 2016.

Olsen, N., Ravat, D., Finlay, C. C., and Kother, L. K. (2017). LCS-1: a high-resolution global model of the lithospheric magnetic field derived from CHAMP and *Swarm* satellite observations. *Geophys. J. Int.*, *211*(3), 1461–1477. https://doi.org/10.1093/gji/ggx381

Ren, Z. Y., Huang, Y. P., Yang, C., Chen, C. J., and Zhang, K. (2025). Preliminary results suggest observations from Macau Science Satellite-1 system can improve knowledge of tidal-induced magnetic fields. *Earth Planet. Phys.*, *9*(3), 586–594. https://doi.org/10.26464/epp2025002

Ronchi, C., Iacono, R., and Paolucci, P. S. (1996). The "cubed sphere": A new method for the solution of partial differential equations in spherical geometry. *J. Computat. Phys.*, *124*(1), 93–114. https://doi.org/10.1006/jcph.1996.0047

Runcorn, S. K. (1975a). An ancient lunar magnetic dipole field. *Nature*, *253*(5494), 701–703. https://doi.org/10.1038/253701a0

Runcorn, S. K. (1975b). On the interpretation of lunar magnetism. *Phys. Earth Planet. Inter.*, *10*(4), 327–335. https://doi.org/10.1016/0031-9201(75)90059-X

Sabaka, T. J., Tøffner-Clausen, L., Olsen, N., and Finlay, C. C. (2020). CM6: a comprehensive geomagnetic field model derived from both CHAMP and swarm satellite observations. *Earth Planets Space*, *72*(1), 80. https://doi.org/10.1186/s40623-020-01210-5

Saltus, R., Alken, P., Balmes, A., Boneh, N., Califf, S., Chulliat, A., Meyer, B., and Nair, M. (2023). Magnetic maps and models for alternative navigation. In *2023 IEEE/ION Position, Location and Navigation Symposium (PLANS)* (pp. 805–813). Monterey: IEEE. https://doi.org/10.1109/PLANS53410.2023.10140025

Stockmann, R., Finlay, C. C., and Jackson, A. (2009). Imaging Earth's crustal magnetic field with satellite data: a regularized spherical triangle tessellation approach. *Geophys. J. Int.*, *179*(2), 929–944. https://doi.org/10.1111/j.1365-246X.2009.04345.x

Thébault, E. (2006). Global lithospheric magnetic field modelling by successive regional analysis. *Earth Planets Space*, *58*(4), 485–495. https://doi.org/10.1186/BF03351944

von Frese, R. R. B., Hinze, W. J., and Braile, L. W. (1981). Spherical Earth gravity and magnetic anomaly analysis by equivalent point source inversion. *Earth Planet. Sci. Lett.*, *53*(1), 69–83. https://doi.org/10.1016/0012-821X(81)90027-3

Wang, J., Shen, X. H., Yang, Y. Y., Zeren, Z., Zhou, B., Werner, M., De Santis, A., Huang, J. P., Yao, C. L., … Lammegger, R. (2023). A global lithospheric magnetic field model between ±65° latitude derived from CSES satellite scalar data. *Phys. Earth Planet. Inter.*, *340*, 107036. https://doi.org/10.1016/j.pepi.2023.107036

Yang, C., Cao, J. W., and Cai, X. C. (2010). A fully implicit domain decomposition algorithm for shallow water equations on the cubed-sphere. *SIAM J. Sci. Comput.*, *32*(1), 418–438. https://doi.org/10.1137/080727348

Yin, L., Yang, C., Ma, S. Z., Huang, J. Z., and Cai, Y. (2017). Parallel numerical simulation of the thermal convection in the Earth's outer core on the cubed-sphere. *Geophys. J. Int.*, *209*(3), 1934–1954. https://doi.org/10.1093/gji/ggx125

Yin, L., Yang, C., Ma, S. Z., Cai, Y., and Zhang, K. (2022). Parallel finite volume simulation of the spherical shell dynamo with pseudo-vacuum magnetic boundary conditions. *J. Computat. Phys.*, *451*, 110866. https://doi.org/10.1016/j.jcp.2021.110866

Yin, L., Ren, Z. Y., Yao, H. B., and Yang, C. (2023). A finite volume method for global electromagnetic induction forward modeling on collocated unstructured grids. *Earth Planet. Phys.*, *7*(1), 57–65. https://doi.org/10.26464/epp2023007

Zhang, K. (2023). A novel geomagnetic satellite constellation: Science and applications. *Earth Planet. Phys.*, *7*(1), 4–21. https://doi.org/10.26464/epp2023019

Zhang, P., Du, J., Yin, L., Yan, Q., Zhang, J., Li, H., Zhang, K., and Chen, C. (2025). A high-resolution lithospheric magnetic field model of China and surroundings by using CHAMP, Swarm, CSES-1, and MSS-1 satellite magnetic measurements and aeromagnetic anomaly data. *Earth Planet. Phys.*, 9(3), 686–696. https://doi.org/10.26464/epp2025057